PERGAMON

International Journal of Heat and Mass Transfer 44 (2001) 771–783

International Journal of HEAT and MASS TRANSFER

www.elsevier.com/locate/ijhmt

# Bubble departure from cavities

Brian K. Mori, W. Douglas Baines*

*Department of Mechanical and Industrial Engineering, University of Toronto, 5 King's College Road, Toronto, ON, Canada M5S 3G8*

Received 1 July 1999; received in revised form 25 March 2000

**Abstract**

An experimental investigation has been undertaken on the growth and departure of bubbles from artificial nucleation sites. Bubbles were produced by gas diffusion from a carbonated water solution on 0.6, 1.48 and 2.08 mm diameter cavities in a horizontal plate. The departure size and growth time of the bubbles produced in the experiments could not be accurately predicted using a force balance analysis and the assumed initial growth condition of a bubble nucleus. A numerical simulation was developed to solve these parameters. This showed that the bubble grows very rapidly after a neck forms. Experiments in which the bubbles grew to a height which was several times the cavity diameter revealed that departure occurred during the rapid growth. The numerical simulation also predicted accurately the volume of the residual bubble inside the cavity and the time until the succeeding bubble appeared above the cavity opening. The effect of surface tension on the bubble departure diameter was found to aid departure by the formation of a bubble neck rather than resisting departure as an adherent force that attached the bubble to the surface. 

## 1. Introduction

In nucleate boiling and in gas release from a supersaturated solution, the departure rate of the formed bubbles controls the heat or mass transport rate. It is thus important to have an understanding of the physics of bubble growth and departure. This is evident from the definitive works of Forster and Zuber [1], Plesset and Zwick [2] and Scriven [3]. They examined bubbles in nucleate boiling where individual bubbles form on a solid surface. This occurs at low temperature differences between the solid and the liquid. The other recognized form, pool boiling, occurs at larger temperature differences. Many analytical studies have been conducted on bubble growth but most have treated the bubbles as both spherical and rigid. A balance of buoyant and surface tension forces was used to set a stability criterion for the bubble departure. The resulting equations have been generally adequate in the prediction of the departure diameters measured in nucleate boiling from small cavities. However, this approach is obviously not valid for large bubbles for which gravity produces an elongated shape. Furthermore, the physics of the departure was not described in detail. The balance of the hydrostatic pressure distribution and surface tension over the height requires that the sum of the curvatures increase with distance from the top of the bubble. In large bubbles, this effect produces a neck close to the surface where the bubble is attached. This has been easily observed in the laboratory and departure appears to be associated with the neck. The neck is not seen in small bubbles but the stresses which produced it must be present in all

* Corresponding author. Tel.: +1-416-978-5737; fax: +1-416-978-7753.

*E-mail address:* baines@mie.utoronto.ca (W.D. Baines).

0017-9310/01/$ - see front matter 
PII: S0017-9310(00)00133-2

**Nomenclature**

| | | | |
|---|---|---|---|
| $a$ | vertical acceleration | $t_d$ | departure time |
| $d$ | diameter of cavity | $x$ | horizontal coordinate measured from $z$ axis |
| $D$ | diffusivity | $z$ | vertical coordinate along the centerline measured from top of bubble |
| $Eo$ | Eotvos number | $V$ | volume of bubble |
| $g$ | acceleration of gravity | $V1$ | volume of bubble producing buoyant force |
| $h$ | height of bubble above top of cavity | $\alpha$ | contact angle |
| $m_a$ | added mass of bubble | $\rho$ | density of water |
| $p_0$ | absolute pressure at top of bubble | $\rho_g$ | density of carbon dioxide |
| $p_v$ | vapor pressure | $\sigma$ | surface tension of water, carbon dioxide interface |
| $r_0$ | radius of curvature at top of bubble | $\theta$ | internal angle of radius of curvature measured from $z$ axis |
| $r_1$, $r_2$ | radii of curvature at any point on the bubble | | |
| $s$ | distance along surface of bubble measured from top | | |

cases. The study described herein examines the formation, growth and departure of large bubbles using a numerical simulation and experiments. The bubbles studied are produced in a supersaturated liquid by gas diffusion. Furthermore, the formation site is a finite cylindrical hole in a horizontal surface. This case has been chosen to simplify the departure problem to its elements. There is ample reason for studying the growth of diffusion bubbles because of the small number of previous studies. The choice of diffusion-driven growth was made here for the simplicity of both experiment and analysis. The bubbles can be produced which are much larger and grow much more slowly than in boiling. Thus, images of the bubbles can be obtained with less sophisticated methods and with greater accuracy. Experiments were video taped from a charge coupled device (CCD) camera and bubble shape profiles were digitized via a computer. The advantage in analysis is the very small magnitude of the forces due to the enlargement and acceleration of the added mass of the bubble. A quasi-steady analysis can be utilized which can be solved with a relatively simple numerical code. It is not necessary to solve the Navier–Stokes equation for the flow field which, although possible, is beyond the scope of this study. These simplifications were adopted primarily to allow clear documentation of the development of the neck and the departure.

The section which follows presents the equations which describe the shape of the bubble as a balance of the static pressure and surface tension forces. The case of a spherical bubble and the criterion which results in bubble departure are also mentioned. Bubble growth by diffusion is calculated using Ficks' law. A brief discussion of the numerical solution technique is included. Section 3 presents the technique for producing and observing the size and shape of diffusion bubbles. The results of the measurements and calculation of bubble shape are discussed in Section 4. Growth rates of the bubbles are treated in Section 5 and the volume and time at departure in Section 6. Section 7 presents some conclusions.

## 2. Bubble shape and growth relations

### 2.1. Bubble shape

This paper addresses very slow growth rates so all the fluid motion terms in the conservation equations are small. The shape is thus defined by Laplace's equation for balance of surface tension force and the pressure difference across the interface. External pressure on the bubble varies hydrostatically and internal pressure is constant. The origin of coordinates is the top where the shape is spherical, so a radius of curvature $r_0$ is specified. At lower elevations, the principal radii of curvature are different. Setting the internal pressure at the vapor pressure of the liquid gives:

$$\rho g z + p_0 - p_v = \sigma\left(\frac{1}{r_1} + \frac{1}{r_2}\right) \tag{1}$$

where $p_0$ is the absolute pressure at the top of the bubble in the liquid, $r_1$ is the radius of curvature which, as rotated, describes the latitude of the bubble. This is centered on the axis. $r_2$ is the radius of curvature in a vertical section of the bubble which, as rotated, describes the longitude. It is co-linear with $r_1$ but the center is different. It may be negative.

At the top of the bubble, the radii are equal. So

$$p_0 - p_v = 2\left(\frac{\sigma}{r_0}\right) \tag{2}$$

This relation provides the initial condition for the numerical integration of Eq. (1). Lengths were made dimensionless by dividing it by $d$ which is the diameter of the cavity. A value of $r_0/d$ is chosen, and the equation is integrated along the coordinate $s$ in the interface. The geometric relations

$$r_1 = \frac{x}{\sin\theta}\frac{\mathrm{d}x}{\mathrm{d}s} = \cos\theta\frac{\mathrm{d}z}{\mathrm{d}s} = \sin\theta \tag{3}$$

connect $x$ and $z$ with $\theta$. Eliminating $r_1$ and $r_2$ from Eqs. (1) and (3) yields a second-order differential equation which was solved numerically using a fourth-order Runge–Kutta routine to produce the bubble shape. This scheme is similar to that used by Chesters [4]. It was chosen for the simplicity of programming and the accuracy was checked for a sphere. The volume of the bubble is calculated from the result by

$$V = 2\pi\int_0^h r_1\sin\theta\,\mathrm{d}z \tag{4}$$

Very small bubbles are spherical because the internal–external pressure difference is much larger than hydrostatic pressure difference. Writing Eq. (1) at the top and base of the bubble gives the difference in the mean radii of curvature at the two elevations as:

$$\frac{1}{2}\left(\frac{r_0}{r_1}+\frac{r_2}{r_2}\right) - 1 = \frac{\rho g r_0 h}{2\sigma} \tag{5}$$

where $h$ is height of the bubble.

For example, setting the difference on the left side as 1% gives:

- the maximum diameter of a full bubble as 0.54 mm
- the maximum diameter of a hemispherical bubble as 0.77 mm

for the shape to be spherical.

Throughout this paper, the analysis is quasi-steady, that is, forces engendered by the motion of the surface are small. The expansion of the gas forces the liquid outward and this requires an additional pressure on the free surface. This can be analyzed as an added mass which is accelerated. In a typical case, this pressure is about 0.001 Pa which is small to the internal pressure from surface tension of 70 Pa.

*2.1.1. Complete bubble*

Integration of Eq. (1) over the full surface of the bubble from the top to the attachment at the base where the diameter, as shown in Fig. 1, is $d$ gives a balance of forces on the bubble. Gauss theorem is employed to convert the surface integral of pressure to a volume integral. This gives an upward buoyant force which is equal to the weight of the water in the volume $V1$ which is outside the cylinder of diameter $d$ and height extending to the bubble surface along with an upward pressure force on the base. Using Eq. (1) and the total volume $V$ as the sum of $V1$ and the central cylinder gives

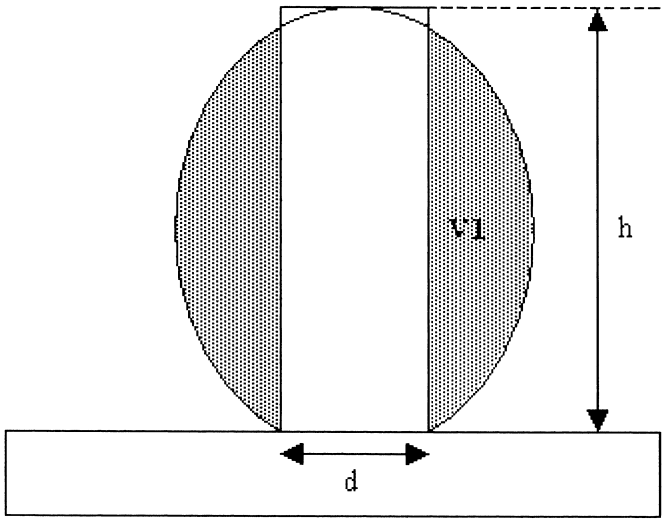


Fig. 1. Definition sketch for buoyant force calculation for an attached bubble.

$$\rho g V - \left[\rho g(h - C_1 r_0) - \frac{2\sigma}{r_0}\right]\frac{\pi d^2}{4} - \pi\sigma d \sin\alpha = (m_a + \rho_g V)a \tag{6}$$

The first term is the buoyancy of an unattached bubble and the second term contains the corrections for the negative buoyancy of the cylinder and the base pressure. The coefficient $C_1$ expresses the shape of the curved upper surface. If it is spherical then

$$C_1 = C_2\left[1 - \left(\frac{2r_0}{d}\right)\right]C_2\left(1 - \frac{C_2}{3}\right) \tag{7}$$

$$C_2 = 1 - \sqrt{1 - \left(\frac{d}{2r_0}\right)^2} \tag{8}$$

which does not give a large correction for bubbles near departure. In the cases measured in this study, it was a maximum of 3%.

The third term in Eq. (6) is the surface tension force. $\alpha$ is the contact angle with the surface. The net force from the left side is equated to the change in momentum of the liquid. The mass $m_a$ is the added mass due to both the expansion and rise of the bubble, and $a$ is the upward acceleration of the bubble.

The standard method for determining bubble departure from surfaces uses this equation with the second term set to zero, a spherical shape and zero acceleration. Beginning with Jakob's [5] application of an equation developed by Fritz [6], this balance has been applied to many cases and with improvements for the force exerted by the acceleration of liquid added mass. A recent attempt was that of Mitrovic [7], which set the pressure difference at the base. This was examined in detail by van der Geld [8], and shown to be invalid, but it did provide an approximation. It is evident that all the detachment criteria based on Eq. (6) cannot be valid because this balance applies at all times. As a demonstration, consider a hemispherical bubble which is growing extremely slowly. The right side of Eq. (6) is set to zero, $h = r_0$, $d = 2r_0$ and $C_1 = 1/3$. Thus, the net buoyant force is zero, and the equation reduces to the sum of the base pressure force and surface tension. With the contact angle $\alpha = \pi/2$, these terms are identical; and this shows that there is an equilibrium. The same result is found for any shape of the bubble for any cross-section. It is concluded that acylation of the added mass and consequent force on the bubble must be included in the analysis before a departure can be explained. Nevertheless, many authors have set the acceleration to zero and equated the first term with the others to set the volume at departure. For example, Eq. (6) gives

$$V = \frac{\pi}{Eo}d^3\left(1 - \frac{d}{2r_0}\right) + \frac{\pi}{4}d^2(h - C_1 r_0)$$
$$Eo = \text{Eotvos number} = \frac{g(\rho - \rho_g)d^2}{\sigma} \tag{9}$$

This relation is similar to the equation derived by van der Geld [8]

$$V = \frac{\pi d^3}{Eo} \tag{10}$$

and also derived analytically by Chesters [4] for small bubbles. None of this type of equation can be used as a rigorous criterion for determining the bubble departure because the forces are either in balance or are defining the added mass acceleration. Thus, each holds exactly in the case of Eq. (9) or approximately in the case of Eq. (10) at all times for the diffusion bubbles studied herein.

### 2.2. Bubble growth rate

A separate calculation was programmed for the rate of gas transfer across the interface. The bubble shape determined by the method described above was the starting point for each time step. Starting with a small spherical shape, the field outside the bubble was divided into a grid and the mass transfer equation was solved in the grid.

$$\frac{\partial C}{\partial t} = D\frac{\partial^2 C}{\partial r^2} + \frac{2}{r}D\frac{\partial C}{\partial r} \tag{11}$$

where $D$ is the diffusivity of gas in water.

This gave the mass transfer rate at the free surface, and a forward difference scheme was employed to set the volume of the bubble at the end of the step. The numerical simulation followed the bubble growth by calculating the shape for this prescribed volume. A value of $r_0$ was assumed and the shape calculated to the elevation where the diameter was $d$. If the volume which resulted did not match the prescribed value, the top radius was adjusted. This was repeated until there was a match. With the new shape, the grid was adjusted to preserve the constant volume of each grid unit. As the bubble grows, the surface of the external volumes are stretched laterally so the thickness decreases. This effect increases the concentration gradient of the gas and, consequently, the mass transfer.

Boundary conditions were the supersaturated concentration of gas far from the bubble and the vapor pressure within the bubble from Eq. (2). An arbitrary initial volume was chosen at the start and the calculation proceeded until the bubble departed. At this point, there was a residual volume in the cavity, so

this was used as the initial condition for the second bubble.

A full description of the simulation and the programs is given by Mori [9].

## 3. Gas diffusion experiments

The objective of the experiments was to study slowly growing bubbles on a fixed cavity. This was achieved using water supersaturated with carbon dioxide in a temperature-controlled environment. The bubble grew from a cylindrical hole on a horizontal stainless steel plate. Carbon dioxide in water was chosen because of its high solubility thus enabling satisfactory bubble growth rates for the temperature range, 10–50°C and the pressure range, 1–5 atm. The resulting bubbles were 2–5 mm in diameter so were readily photographed with a CCD camera linked to a standard VCR (video camera recorder). Images were recorded at the standard 30 frames/s. A lens with bellows was employed to give an image which occupied most of the frame. Later, the recorded images were digitized as GIF files using a frame grabber and stored on personal computer discs for analysis. No corrections to the image were required for the diffraction through the cylindrical surface because there was water on both sides of the glass cylinder and an external plane viewing surface.

The pressure vessel, shown in Fig. 2, was made by clamping a glass cylinder of internal diameter 49.45 mm, length 100 mm between two stainless steel plates. A rubber O-ring was used to seal the glass joint. The glass cylinder was designed to withstand 10 atm pressure. A square cylinder fabricated from acrylic plastic surrounded the glass cylinder and water circulated between the two. This came from a continuously circulating loop supplied by a pump. The loop passed though a water bath with thermostatic controls. Temperature of the supply water and loop were monitored continuously. The difference between these was 0.2°C or less during the experiments.

The lower end plate had a raised section so that the camera had an unobstructed view of the base of the bubble. The cylindrical cavity was drilled mechanically in the center of the raised metal surface and this served as the nucleation site. A separate plate with a different cavity diameter was dropped into the cylinder for two other tests. In both cases, the cavity radius was determined by photography.

Two supply tubes passed through the upper plate. One carried distilled water and the other carried carbon dioxide gas from a high pressure tank through a regulator (Matheson 3104A) inlet and outlet two pressure gauges. The water in the glass cylinder was initially pressurized at several atmospheres and the test temperature for long enough to full saturation. At the start of a test, the gas was depressurized to an atmospheric one. This unstable condition produced a gas bubble at the prepared site and, on some occasions, at other natural sites. A sequence of 6–10 bubbles were then recorded on videotape.

The scale of each image was obtained by measuring the width of the cavity in the frame. Before the apparatus had been sealed, the hole was viewed perpendicular to the axis and a standard scale was included in the

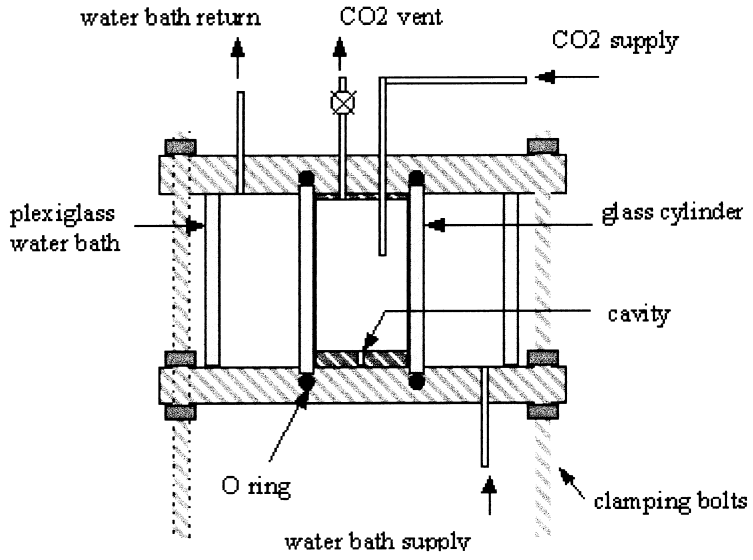


Fig. 2. Cross-section of pressure vessel used in bubble growth experiments.

image. The edge of the bubble was easily seen to an accuracy of 1/2 pixel on the monitor screen, and the pixel location was determined using software written for this project. This dimension when compared to the diameter of the cavity indicates an accuracy of 2%. Width, height and volume were calculated from the pixel interval and scaling. After inception, the bubble shape was a spherical sector which expanded with

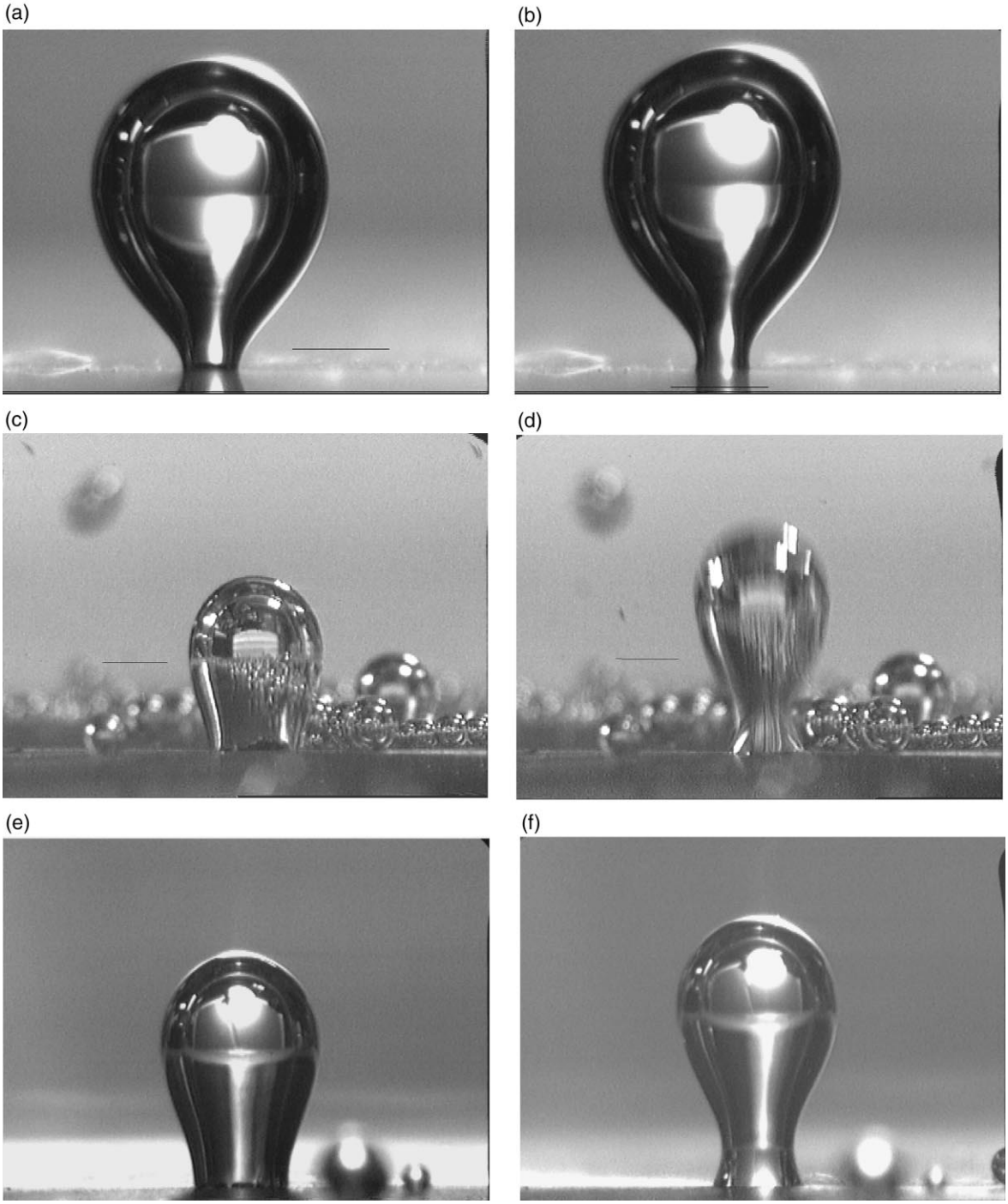


Fig. 3. Comparison of the bubble neck formation for cavity diameters of $d = 1.43$ mm (upper) and $d = 2.08$ mm (lower).

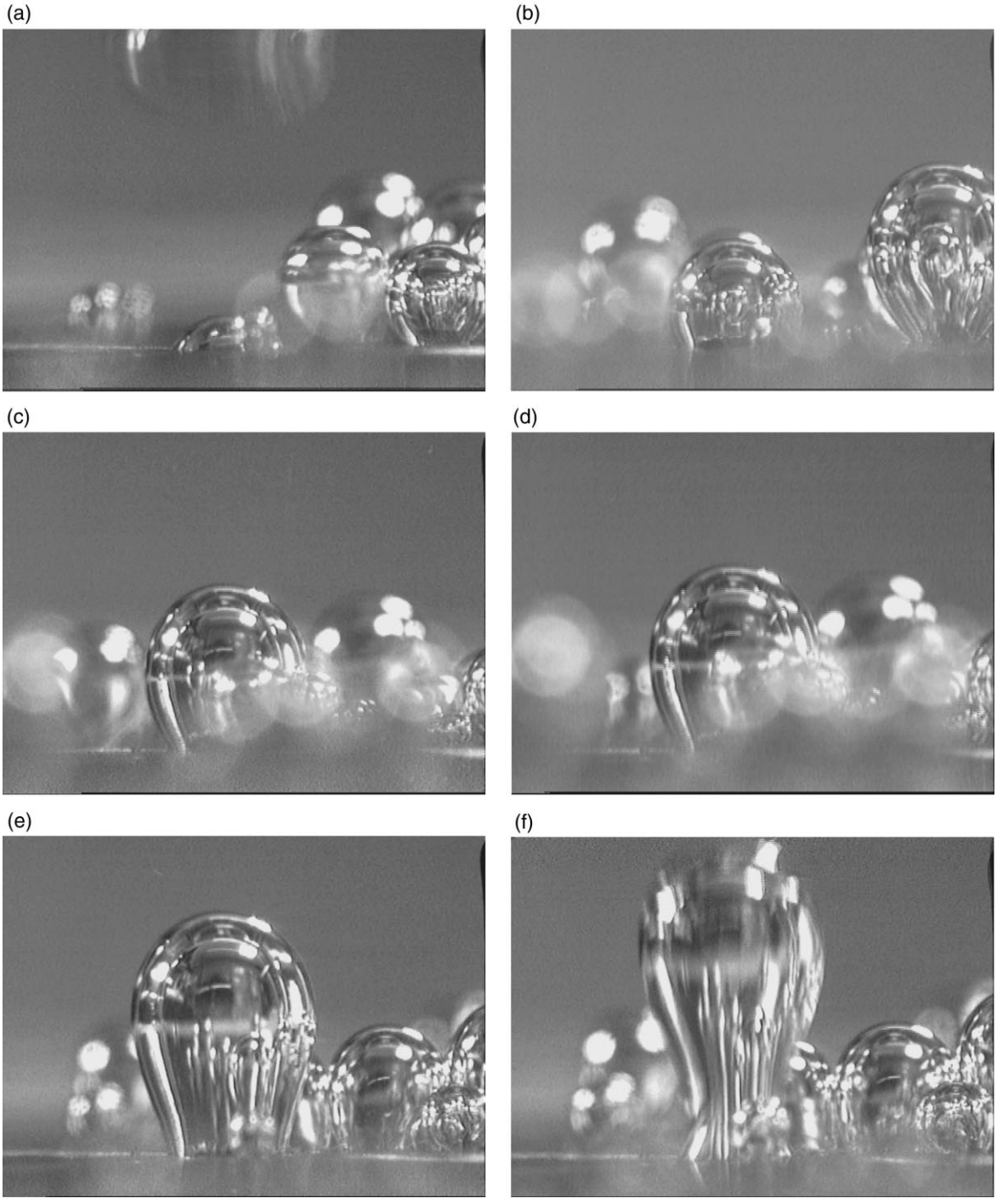


Fig. 4. Photos of bubbles on the cavity with $d = 2.08$ mm during growth in a typical test. Time is (a) 0 s, departing bubble seen at the top, (b) 40 s, (c) 70 s, (d) 90 s, (e) 105 s and (f) 107 s.

time. At some point after the bubble was larger than a hemisphere, the shape became elongated vertically. The stretching extended until the time of detachment. Immediately before detachment, a neck or narrowing is formed near the cavity, as can be seen in Fig. 3. The sets of photos show bubbles attached to the cavities of diameter $d = 0.6$, 1.43 and 2.08 mm. The images on the left show the neck formation, and those on the right are the last ones recorded before detachment. In the largest cavity, the neck collapsed at a section above the surface leaving a small bubble which extended above the solid surface. However, no neck or residual bubble was visible on the smaller ones. However, it was deduced from the time interval between departure and appearance of a bubble top that there must have been a residual bubble inside it. This waiting time was predicted accurately by the numerical simulation.

## 4. Bubble shape

As the bubble grew from the cavity, the shape changed from spherical to ovoid with the height greater than the width and then to a neck. Soon after the neck appeared, the bubble center accelerated upward and it departed. The shape progression is shown in the series of photos in Fig. 4. The deviation from sphericity can be determined quantitatively by plotting the volume as a function of height, as shown in Fig. 5. The solid curve is the height of a sphere attached to a cavity of diameter $d$ as a function of the volume. Points are the mean heights measured from the images.

Vertical bars show the range of individual measurements. The deviation from sphericity starts at a height of 1.9 mm which is a bubble radius of 1.07 mm for the cavity diameter of 1.46 mm. This is about four times the value given by Eq. (5) for a 1% variation of hydrostatic pressure over the height of the bubble. This shows that the pressure must deviate from uniform by a much larger value than 1% for the non-spherical shape to be evident in the image and the integral properties of the bubble.

Fig. 6a and b present a comparison of the measured and calculated bubble shapes as a function of time. The points are scaled from the photos and the lines are the results of the numerical simulati. Time was measured from the departure of the antecedent bubble. In the numerical simulation, the volume at time zero was taken to be the volume of the bubble below the neck at the break-off. The comparison is generally good but, at later times, the top of the measured bubble is flattened slightly as compared to the prediction. This is an artifact of this particular set of images.

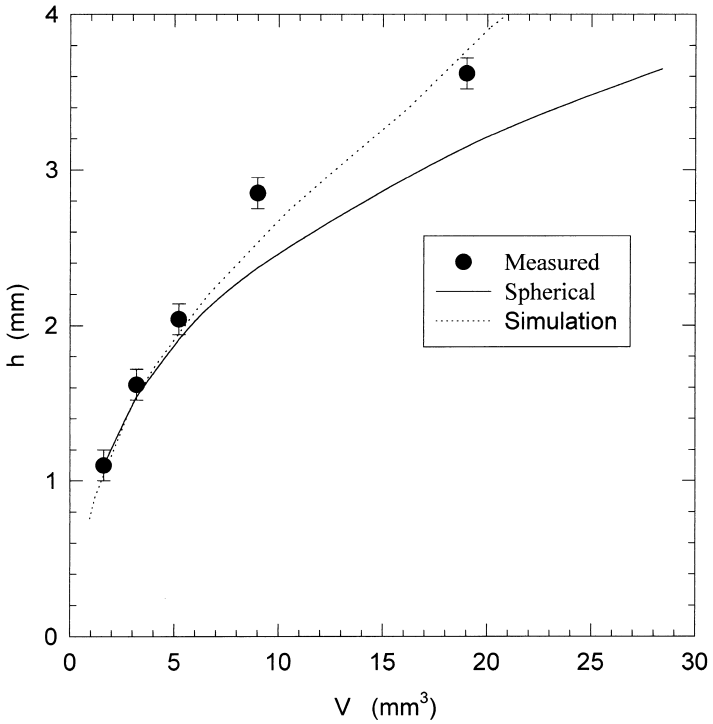


Fig. 5. Plot of bubble height as a function of volume for the test with $d = 1.46$ mm. Carbon dioxide gas in water, temperature = 9.87°C, gas saturation pressure = 6.24 atm. Points are measurements, line is height for a sphere of the same volume.

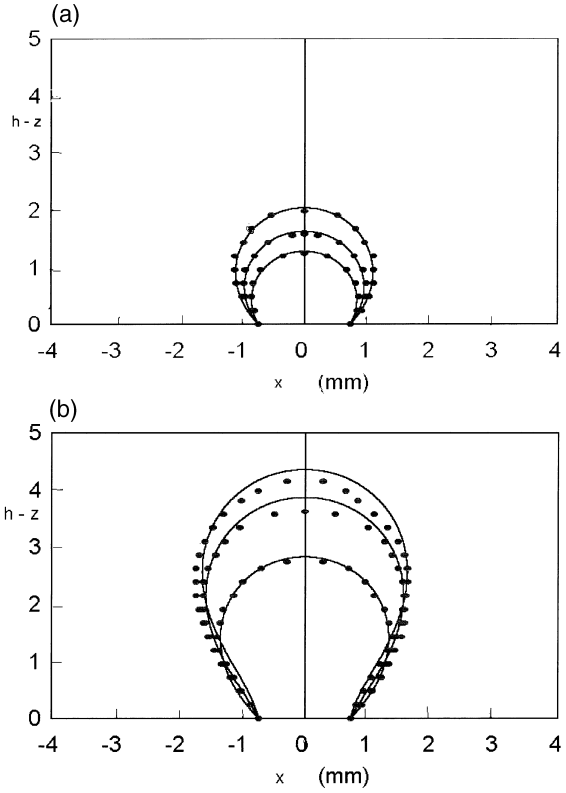


Fig. 6. Plots of bubble cross-section for $d = 1.46$ mm. Carbon dioxide gas in water, temperature = 9.87°C, gas saturation pressure = 6.24 atm. Points are measured and lines are from numerical simulation. (a) Spherical shapes at $t = 9$, 11 and 13 s. (b) Ovoid shapes at $t = 17$, 21 and 22.5 s.

A distortion was produced by the VCR which flattened the top of the image. This was rectified for the images used for volume measurements.

## 5. Bubble growth

In each test, six or eight bubbles were measured from the video images and the volume calculated by numerically integrating the horizontal cross-section area. In each test, there was a small variation in growth rate, and the height and volume at departure. A typical test is summarized in Fig. 7, where the volume growth is plotted. The vertical bars on the experimental points show the extreme values of the eight bubbles. The line is the numerical simulation. The agreement is close. In other tests, the two coincided. On the vertical axis, the volume of the bubble above the top of the cavity is plotted. For the simulation, the gas volume in the cavity at time zero was determined by calculating backwards from the time at which the top of the bubble was seen at the top of the cavity. This was necessary for $d = 1.46$mm tests because the bubble separated just below the line of sight and the residual bubble could not be seen. The average level of the top of the bubble was calculated by this scheme to be 0.535 mm, so the bubble grew by 1.98 mm$^3$ before it could be seen. The waiting time, which was 7.6 s for this test, varied with the water temperature and gas saturation pressure. However, the water volume in the cavity was 1.98 mm$^3$ in each case. Waiting time was the interval between departure of a bubble and appearance of the top of the following one at the top of the cavity.

The waiting time was more readily determined in the analysis of the large cavity. Fig. 8 is the image taken just at departure. The neck is clearly visible and the spherical shape of the section is in contact with the cavity wall. As the bubble grows further, the neck moves downward; and at departure, the interface breaks at the neck. The residual bubble from which the next one grows is the volume below the neck upon breaking. This bubble retreats into the cavity and the top is not seen in the waiting time, that is, until diffusion has produced growth to the top of the opening.

## 6. Bubble departure

This is a rapid process, even for these slowly growing bubbles. Fig. 9a–d are frames taken 1/30 s apart as the event occurred. The neck is just visible in the third photo and the bubble has departed in the fourth one.

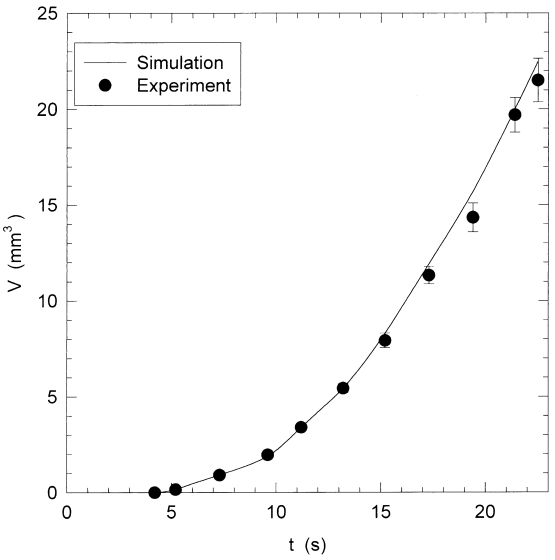


Fig. 7. Bubble volume as a function of time since departure of the antecedent bubble. Temperature = 19.97°C, gas saturation pressure = 5.29 atm. Curve is the numerical simulation, points are measured.

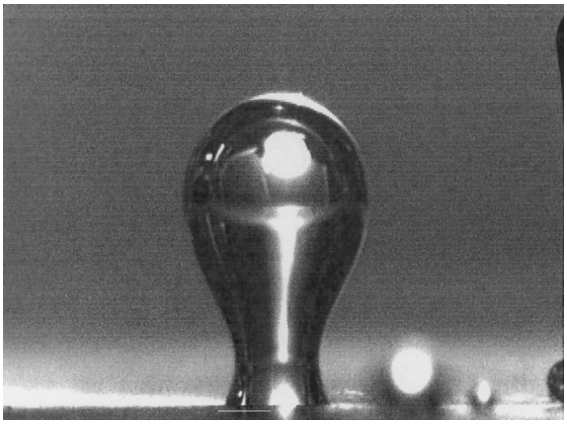

Fig. 8. Bubble at departure from the large cavity.

Detailed comparison of the shapes reveals that the top radius is larger in the second photo than in the first one but it is the same in the third and second photos. This is explained by following the shape, volume and height throughout the bubble growth. As the volume increases by diffusion, the radius increases. At the start, the shape is a spherical sector which expands to a rough hemisphere for which the contact angle is $\pi/2$. Then, as the bubble expands, the contact angle decreases. This neck development was followed in the numerical simulation but no break in the free surface ensued.

First, consider the numerical solution for a large top radius plotted in Fig. 10. The edge of the cavity at $x/d = 0.5$ could be found at three values of $z/d$. The smallest, $z/d = 0.18$, is for a spherical sector, and this would be seen as the bubble emerges from the cavity. The second, $z/d = 2.10$, would be the shape of the bubble attached to the top edge of the cavity, and the third would be the bubble attached at both the edge and at the cavity inside the wall. It was seen in every case that the bubble grew from the hemispherical shape to the second case with steadily increasing top radius. Then, suddenly it detached at the top edge and attached on the wall at the $z/d$, for the largest $z/d$.

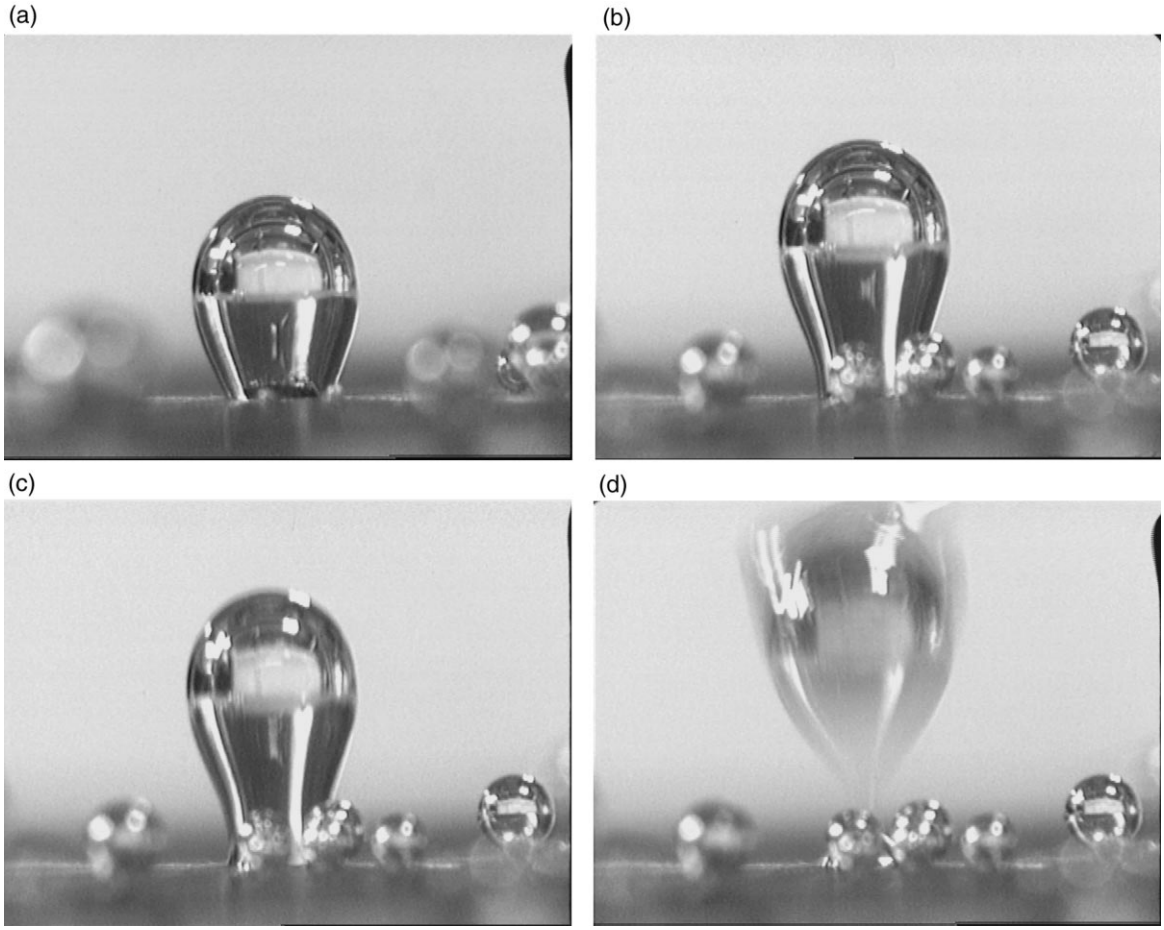


Fig. 9. Images of bubble departure taken 1/30 s apart. Conditions as given in Fig. 8.

There was no change in the bubble volume above the wall for this jump. As diffusion continued and the volume increased, the attachment point rose in the cavity so the neck could be seen above the surface, as shown in Fig. 8. The shape was maintained with this volume increase and would have continued until contact was at the edge. However, the bubble detached before or as the edge was reached. A good approximation of the detachment time is, thus, the instant at which the lower contact point was at the edge. The numerical simulation does not produce detachment, and if it is continued beyond the edge attachment, it produces a top radius increase and the neck descent until the neck radius $x/d = 0.5$. Here, it is at the edge. Any increase in volume and top radius requires $x/d > 0.5$, so the attachment point is on the wall outside the cavity. This was not seen in any of the cases. Fig. 11 is a plot of the height as a function of volume for the three attachment levels. The open squares follow the growth to the hemisphere, and the open circles follow the growth of the second height value. The solid circles are the heights for the largest value of $z/d$. The dashed line shows the volume–height relation as the attachment point rises inside the cavity. It could connect the upper and lower lines at any location. However, the experiments indicated that this occurred for a contact angle of 78°. The limiting volume for attachment with the cavity is the maximum volume on the right. The height for this case is less than that after the jump. Detachment might be produced by the force of the added mass which, although small, would have to be negative in this region.

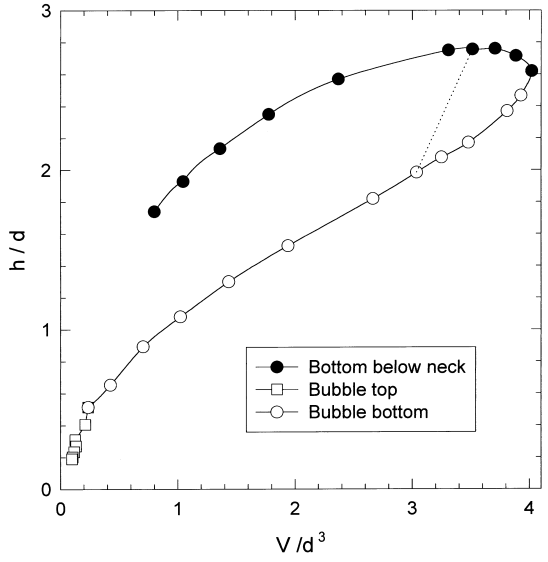


Fig. 11. Volume of bubble as a function of height for $Eo = 0.600$and $x/d = 0.5$. Top radius $r_0/d$ varies from 0.5 to 0.802. Contact points are intersections with dotted lines in Fig. 10. Dashed line shows jump of contact point at neck formation.

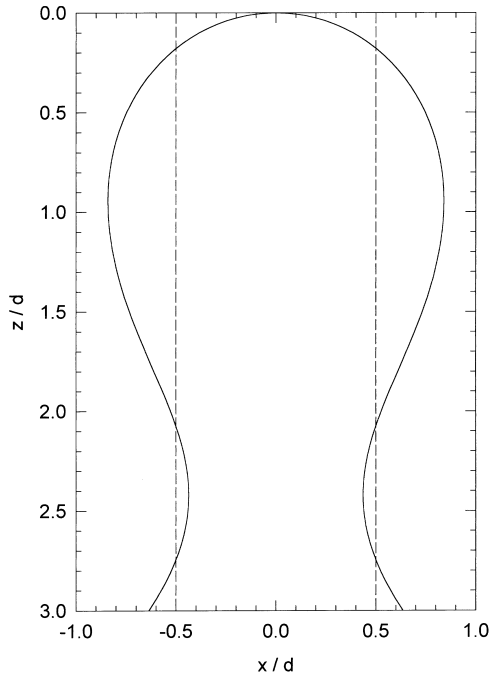


Fig. 10. Bubble shape as calculated for $Eo = 0.600$, $r_0/d = 0.780$. Dotted line is $x/d = 0.5$, which is edge of the cavity.

Writing Eq. (9) for the neck cross-section using the dimensionless variables gives a relation for the depar-

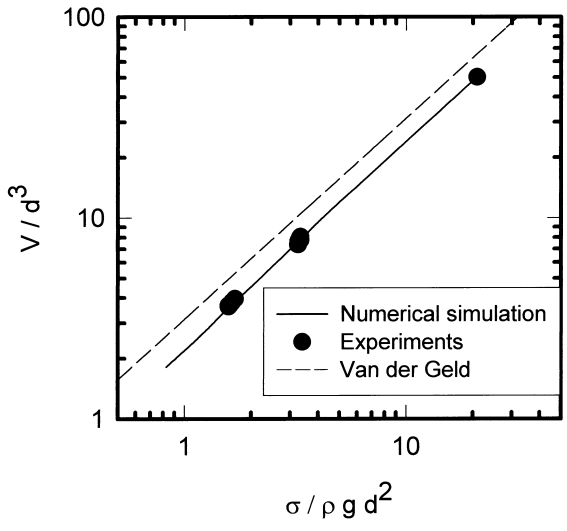


Fig. 12. Bubble volume at departure. Points are measurements and solid line is numerical simulation of large bubbles. Dotted line is Eq. (10) which was developed for small cavities.

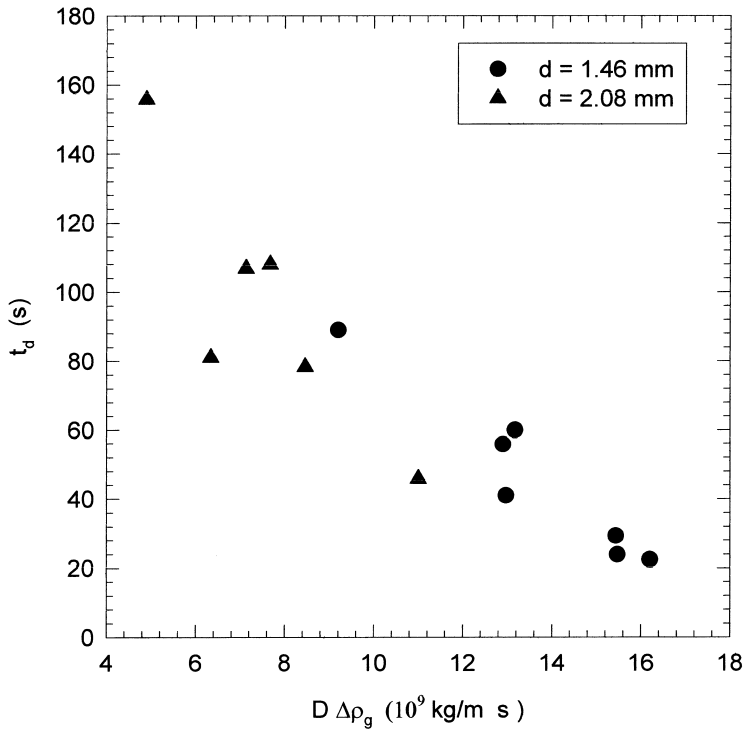


Fig. 13. Measured time interval between departures as function of the mass transfer driving potential.

ture volume in terms of the neck dimensions:

$$V_n = \frac{\pi}{Eo}\frac{d_n}{d}\left(1 - \frac{d_n}{2_{r_0}}\right) + \frac{\pi}{4}\left(\frac{\pi}{Eo}\right)^2\frac{h_n}{d} \tag{12}$$

where the subscript $n$ denotes the property at the neck.

This agreement and the calculation which showed that the hydrodynamic forces were much smaller than the buoyant and surface tension forces indicate that the shape is well described by the quasi-steady approximation. Thus, the simulation was used to set values of the volume and time at departure. The volume was taken to be that at the neck. For quasi-steady growth, the bubble volume at departure would depend only on the variables noted above, that is, buoyancy,

$$\frac{V}{d^3} = fcn(Eo, \alpha)$$

cavity diameter and surface tension.

Since the contact angle is $\pi/2$ at the neck, the sine is unity. Measurements of the volume in the last frame before departure gave the mean values of the parameters plotted in Fig. 12 for the mean of 10 bubbles. The results of the numerical simulation using the volume at the neck are also shown in this plot. The solid line is the plot of these calculations. The dashed line is Eq. (10) which lies above the measured and calculated values. Inasmuch as Eq. (10) was derived for small bubbles, it would not be expected that it would apply to large ones. In the range of these studies, the volume is about 2/3 of that given by Eq. (10). There does not appear to be an approach to it as bubble size decreases. Inserting the calculated or measured values for the neck in Eq. (12) gives a prediction for the volume at departure. These are identical to the values given in Fig. 12 as would be expected. Both were formed from the numerical solution.

Although the numerical solution can be used to define the volume at departure, yet the mechanics of departure have not been explained. All the published analyses use the force balance of buoyancy and surface tension, but this has been shown to be an invalid approach. It will probably be necessary to include the liquid motion in the analysis to provide this explanation. A significant fact noted in the numerical simulation was that the height of the bubble does not grow after the bottom of the neck region reaches the edge of the cavity. This indicates that the water ahead of the bubble would decelerate and, hence, produces a negative pressure on the top. This could change the shape of the bubble and, in particular, the neck so that it would sufficiently reduce in size to close the neck.

The time of departure, which is the time interval for bubble attachment, is controlled by the rate of diffu-

sion of gas from the environment. It thus increases with both the diffusivity $D$ and the difference in density of the gas in the environment and in the bubble $\Delta\rho_g$. The product of these is the driving potential for mass transfer. The plot of measured departure times for all the experiments in Fig. 13 demonstrates that cavity size has little, if any, influence on the mass transfer.

## 7. Conclusions

A numerical simulation of the growth of a diffusion driven bubble has been developed and solved. It uses the Laplace equation for the bubble surface boundary condition and the radial mass transfer approximation for the surface mass transfer. Two standard forward difference schemes are used to integrate the relations. The results agree well with a series of experiments of carbon dioxide bubbles in water. It is concluded that this simple approach is valid and can be applied to many other cases. For example, diffusion bubbles which nucleate from very small surface cavities could be solved if the contact angle can be well defined. The scheme has already been applied to vapor bubbles in a superheated liquid with good results. These calculations will be reported in another paper.

The experiments and simulation demonstrate that the volume at detachment is not described by a force balance but can be set by the Eotvos number, which is a dimensionless number containing buoyancy, surface tension and cavity diameter. Numerical values obtained in the experiments confirm those from the simulation. It is hoped that this approach will simplify the analysis of nucleate boiling.

## Acknowledgements

This research was supported by the Natural Sciences and Engineering Research Council of Canada under Grant A-1066. This assistance is gratefully acknowledged.

## References

[1] H.K. Forster, N. Zuber, Growth of a vapor bubble in a superheated liquid, J. Appl. Phys. 25 (4) (1954) 474–478.
[2] M.S. Plesset, S.A. Zwick, The growth of vapor bubbles in superheated liquids, J. Appl. Phys. 25 (4) (1954) 493–500.
[3] L.E. Scriven, On the dynamics of phase growth, Chem. Eng. Sci. 10 (2) (1959) 1–13.
[4] A.K. Chesters, An analytical solution for the profile and volume of a small drop or bubble symmetrical about a vertical axis, J. Fluid Mech. 81 (4) (1977) 609–624.
[5] M. Jakob, Heat Transfer, vol. 1, Wiley, New York, 1959.
[6] W. Fritz, Berechnung des maximal volumen von dampfblasen, Phys. Z. 36 (1935) 379–384.
[7] J. Mitrovic, Das abreissen von dampfblasen an festen heizflachen, Int. J. Heat Mass Transfer 26 (1983) 955–963.
[8] C.W.M. van der Geld, Bubble detachment criteria: some criticism of 'Das Abreissen von Dampfblassen an festen Heizflachen', Int. J. Heat Mass Transfer 39 (1996) 653–667.
[9] B.K. Mori, Studies of bubble growth and departure from artificial nucleation sites, Ph.D. Thesis, Department of Mechanical and Industrial Engineering, University of Toronto, 1998.